Electron charge qubits on solid neon with 0.1 millisecond coherence time

Xianjing Zhou,[1,2,*] Xinhao Li,[1,*] Qianfan Chen,[1] Gerwin Koolstra,[3] Ge Yang,[4,5] Brennan Dizdar,[6] Xu Han,[1] Xufeng Zhang,[7] David I. Schuster,[2,6,8,†] and Dafei Jin[1,2,9,‡]

[1] *Center for Nanoscale Materials, Argonne National Laboratory, Lemont, Illinois 60439, USA*
[2] *Pritzker School of Molecular Engineering, University of Chicago, Chicago, Illinois 60637, USA*
[3] *Computational Research Division, Lawrence Berkeley National Laboratory, Berkeley, California 94720, USA*
[4] *The NSF AI Institute for Artificial Intelligence and Fundamental Interactions, USA*
[5] *Computer Science and Artificial Intelligence Laboratory, Massachusetts Institute of Technology, Cambridge, Massachusetts 02139, USA*
[6] *James Franck Institute and Department of Physics, University of Chicago, Chicago, Illinois 60637, USA*
[7] *Department of Electrical and Computer Engineering, Northeastern University, Boston, Massachusetts 02115, USA*
[8] *Department of Applied Physics, Stanford University, Stanford, California 94305, USA*
[9] *Department of Physics and Astronomy, University of Notre Dame, Notre Dame, Indiana 46556, USA*

(Dated: 25 October 2022)

Electron charge qubits are appealing candidates for solid-state quantum computing because of their compelling advantages in design, fabrication, control, and readout. However, electron charge qubits built upon traditional semiconductors and superconductors are historically known to suffer from a short coherence time that hardly exceeds 10 microseconds. The decoherence primarily arises from the inevitable charge noise in conventional host materials. Here, we report our experimental realization of ultralong-coherence electron charge qubits based upon a unique platform that we recently developed. Such qubits utilize the motional states of isolated single electrons trapped on an ultraclean solid neon surface in vacuum and strongly coupled with microwave photons in an on-chip superconducting resonator. The measured relaxation time T_1 and coherence time T_2 are both on the order of 0.1 millisecond. The single-shot readout fidelity without using a quantum-limited amplifier is 97.5%. The average one-qubit gate fidelity using the Clifford-based randomized benchmarking is 99.95%. Simultaneous strong coupling of two qubits with the same resonator is demonstrated, as a first step toward two-qubit entangling gates for universal quantum computing. These results manifest that the electron-on-solid-neon (eNe) charge qubits have outperformed all the existing charge qubits to date and rivaled the state-of-the-art superconducting transmon qubits, holding promise as ideal qubits for a scalable quantum computing architecture.

Quantum bits (qubits) are the fundamental building blocks in quantum information processing. A key measure of a qubit's performance is its coherence time, which describes how long a superposition between two quantum states $|0\rangle$ and $|1\rangle$ can persist [1]. Among a handful of on-chip solid-state qubits today [2,3], a coherence time on the order of 0.1 ms or longer has only been achieved in the semiconductor quantum-dot and donor qubits based on electron spins [4–6], and superconducting transmon and fluxonium qubits based on capacitively and inductively shunted Josephson junctions [7–10]. By contrast, the coherence time in the traditional semiconductor quantum-dot qubits and superconducting Cooper-pair-box (CPB) qubits based on electron charges is at most on the order of 1 μs [11,12]. To our knowledge, no electron charge qubits in any existing platforms have exhibited a coherence time longer than 10 μs. Given the typical one-qubit gate time around 10 ns in these systems, it is imperative for charge qubits to reach a coherence time on the order of 0.1 ms or longer (a ratio of $\gtrsim 10^4$ between coherence time and gate time) to make them serious contenders for quantum computing [13].

The short coherence time for traditional electron charge qubits is generally recognized as a result of their high sensitivity to environmental noise, *e.g.*, charge fluctuations in the host materials or control apparatus [14,15]. Nonetheless, if their coherence time can be significantly prolonged, electron charge qubits will possess unparalleled advantages: (i) They can be conveniently designed and fabricated with no need of spin-purified substrates or patterned micromagnets, substantially reducing the manufacturing cost [16]. (ii) They can be electrically controlled with no involvement of magnetic field, inherently eliminating the compatibility issue between magnetic field and superconducting circuits [17]. (iii) They can be individually addressed and readout by microwave photons thanks to the much stronger coupling between an electric dipole and electric field than a magnetic dipole and magnetic field, fundamentally avoiding the concern of high microwave power or complex spin-charge conversion [18].

In our recent work [19], we reported our experimental realization of a new qubit platform based upon isolated single electrons trapped on a solid neon surface in vacuum. Neon (Ne), as a noble-gas element, is inert against forming chemical bonds with any other elements. In a low-temperature and near-vacuum environment, it spontaneously condenses into an ultrapure semi-quantum solid [20] devoid of any two-level fluctuators (TLFs) or quasiparticles that are present in most conventional materials [17,21]. Its small atomic polarizability and negligible spinful isotopes make it akin to vacuum with minimal charge and spin noise for electron qubits [20,22]. By integrating an electron trap in a circuit quantum

electrodynamics (cQED) architecture, we achieved strong coupling between the charge (motional) states of a single electron and a single microwave photon in an on-chip superconducting resonator. Qubit gate operations and dispersive readout were implemented, which determined the relaxation time T_1 of 15 μs and coherence time T_2 around 200 ns.

In this paper, we report our latest experimental breakthroughs on the electron-on-solid-neon (eNe) qubit platform. By adjusting the neon-growth condition, stabilizing the gate-electrode potential, and working at the charge sweet spot, we successfully extend both T_1 and T_2 to 0.1 ms time scale, corresponding to respectively 10 and 1000 times of improvement to our previous results. In addition, we perform single-shot readout of the qubit states [23] and obtain a 97.5 % readout fidelity without using a quantum-limited amplifier. This is comparable with the readout fidelity of the state-of-the-art transmon qubits with a similar amplification chain. We also perform the Clifford-based randomized benchmarking [24] and obtain an average one-qubit gate fidelity of 99.95 %, which is well above the fault-tolerance threshold for quantum error correction with surface codes [25]. Furthermore, we manage to simultaneously couple two electron qubits with the same resonator, as a first step toward two-qubit entangling gates for universal quantum computing [26]. All these results suggest that the eNe qubits have outperformed all the traditional semiconductor and superconducting charge qubits and rivaled the best superconducting transmon qubits today.

Qubit design and spectroscopy

The eNe qubit is situated in a niobium (Nb) superconducting quantum circuit that is fabricated on an intrinsic silicon (Si) substrate, as shown in Fig. 1a. A channel of 3.5 μm in width and 1 μm in depth is etched into the substrate. A quarter-wavelength double-stripline microwave resonator runs on the bottom through the channel. A dc electrode, called the trap, also runs on the bottom, but from the other end of the channel into the open end of the resonator. The channel, resonator, and trap are all deformed into oval shapes in the trapping region to accommodate the desired functionalities as described below. On the ground plane outside the channel, four additional dc electrodes, made into two pairs and called the resonator-guards and trap-guards respectively, surround the trapping region. The dc bias voltages applied to all the dc electrodes, as well as the resonator with its tuning-fork structure [27], tune the electron trapping potential. The qubit states $|0\rangle$ and $|1\rangle$ are defined by the electron's motional (charge) states, *i.e.*, the ground state $|g\rangle$ and the first excited state $|e\rangle$ respectively, in the y-direction across the channel. The electric dipole transition between $|g\rangle$ and $|e\rangle$ strongly couples with the electric field, which points from one stripline to the other, of the microwave photons in the antisymmetric (differential) mode of the resonator [19,27]. The bare resonator frequency, defined after the neon filling but before the electron-photon coupling, is $\omega_r/2\pi = f_r = 6.4262$ GHz. The resonator linewidth is $\kappa/2\pi = 0.46$ MHz, which is dominated by the input and output photon coupling. All the microwave measurements are done in a transmission configuration through the resonator.

We fill a controlled amount of liquid Ne into the sample cell, using a homemade gas-handling puff system, to wet the channel and quantum circuit at around 26 K. We cool the system down along the liquid-vapor coexistence line and turn the liquid into solid by passing the solid-liquid-gas triple point at the temperature $T_t = 24.6$ K and pressure $P_t = 0.43$ bar [28]. We hold the temperature at 10 K for 1 – 2 hours to anneal the solid and smooth out the surface [29], and then continuously cool down to the base temperature around 10 mK for experiments. The thickness of solid Ne that covers the trapping region is estimated to be tens of nanometers. Electrons are emitted from a heated tungsten filament above the quantum circuit and are trapped on the solid Ne surface under the combined actions of natural surface potential and applied electric potential [19,20,30].

Our electron-photon (qubit-resonator) coupled system is a typical cQED system, whose schematic spectrum is shown in Fig. 1b. When the qubit and resonator are uncoupled, the qubit has its bare frequency $\omega_q/2\pi = f_q$. In the presence of a finite coupling strength g, the eigenstates of the coupled system are dressed states[18]. In the resonant regime, $f_r = f_q$, the qubit and resonator maximally hybridize, and a vacuum Rabi splitting $2g$ opens up. In the dispersive regime, the detuning $|\Delta = \omega_q - \omega_r| \gg g$, the actual qubit frequency acquires a shift of $(1 + 2\bar{n})\chi$, in which χ is called the dispersive shift, $2\bar{n}\chi$ is called the ac Stark shift, and $\bar{n}$ is the average intra-resonator photon number, meanwhile, the actual resonator frequency acquires a $+\chi$ or $-\chi$ shift, when the qubit is kept in the excited or ground state, respectively.

We first verify the strong coupling between a trapped single electron and a microwave photon. By varying the resonator-guard voltage V_{rg} and keeping all other voltages fixed, we tune the qubit frequency f_q across f_r. The normalized transmission amplitude $(A/A_0)^2$ through the resonator is plotted in Fig. 1c. Two avoided crossings, known as the vacuum Rabi splitting, can be clearly seen. A line cut in Fig. 1c at the on-resonance condition $f_q = f_r$, marked by the pink arrows, is plotted in Fig. 1d. By fitting the curve with the input-output theory, we obtain the electron-photon (qubit-resonator) coupling strength $g/2\pi = 2.3$ MHz, and the on-resonance qubit linewidth $\gamma/2\pi = 0.36$ MHz. The fact that $g > \kappa > \gamma$ indicates that the qubit and resonator are strongly coupled and that the qubit dephasing is slower than the photon decay. In this vacuum Rabi splitting measurement, $\bar{n}$ is kept below 1, as can be verified by the ac Stark effect described below [31].

We use the two-tone qubit spectroscopy to reveal the qubit spectrum tuned by V_{rg}. A probe tone at a fixed probe frequency $f_p = f_r$ and a drive tone with a variable drive frequency f_d around f_r are sent into the system together. The transmission phase ϕ through the

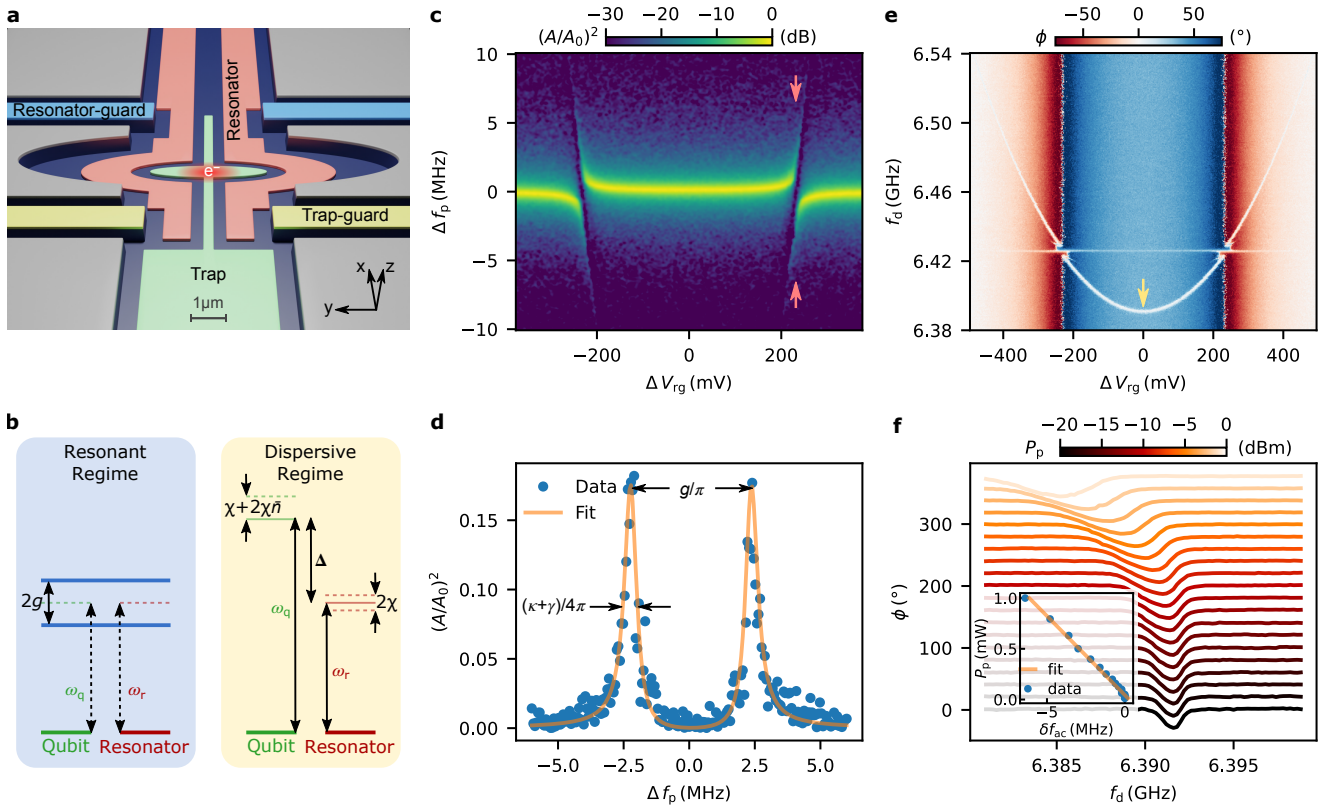

Fig. 1. Spectroscopic characterization of the electron-on-solid-neon (eNe) charge qubit. **a**, Schematic of the device. A single electron is trapped on a solid Ne surface in the oval region of the channel. Its qubit spectrum is tuned by the dc electrodes around and its motional states in y are coupled with the electric field of microwave photons in the double-stripline resonator. **b**, Schematic of the qubit-resonator coupled spectrum. $\omega_q = 2\pi f_q$ is the bare qubit frequency, $\omega_r = 2\pi f_r$ is the bare resonator frequency, and g is the coupling strength. In the resonant regime, $f_r = f_q$, the qubit and resonator hybridize and a vacuum Rabi splitting $2g$ opens up. In the dispersive regime, the detuning $|\Delta = \omega_q - \omega_r| \gg g$, the actual qubit frequency exhibits the dispersive shift χ and the ac Stark shift $2\chi\bar{n}$, in which $\bar{n}$ is the average intra-resonator photon number, whereas the actual resonator frequency exhibits a $+\chi$ or $-\chi$ shift, when the qubit is kept in the excited or ground state, respectively. **c**, Observation of vacuum Rabi splitting. The normalized microwave transmission amplitude $(A/A_0)^2$ through the resonator is plotted versus the offset probe frequency $\Delta f_p = f_p - f_r$ and the offset resonator-guard voltage $\Delta V_{rg} = V_{rg} - V_{ss}$, where V_{ss} is the value of V_{rg} on the sweet spot pointed by the yellow arrow in **e**. The pink arrows mark the on-resonance condition when $f_q = f_r$. **d**, Line plot of $(A/A_0)^2$ versus Δf_p at the value of V_{rg} indicated by the pink arrows in **c**, where the qubit and resonator are on resonance, $f_q = f_r$. The two peaks give the coupling strength g and the qubit linewidth γ when $f_q = f_r$. **e**, Measurement of qubit spectrum. The microwave transmission phase ϕ through the resonator probed at the bare resonator frequency, $f_p = f_r$, is plotted versus the drive frequency f_d and ΔV_{rg}. The white curve shows the nearly quadratic dependence of qubit frequency f_q on ΔV_{rg}. The yellow arrow indicates the minimum called the charge sweet spot. **f**, Observation of the ac Stark shift. The transmission phase ϕ at $f_p = f_r$ is plotted versus f_d and probe power P_p, when the qubit is on the sweet spot in **e**. With increasing P_p, the qubit frequency is red-shifted due to the ac Stark effect. In the inset, the frequency shift δf_{ac} shows a linear dependence on P_p (equivalent to the average intra-resonator photon number $\bar{n}$).

resonator is plotted in Fig. 1e. The dependence of f_q on V_{rg} can be identified as the white curve, where f_d hits f_q and induces a sudden phase shift. The spectrum suggests that f_q is nearly a quadratic function of V_{rg} and contains a minimum at the so-called charge sweet spot, as indicated by the yellow arrow. On this spot, where $f_q = f_{ss} = 6.3915\,\text{GHz}$ and $V_{rg} = V_{ss} = -270\,\text{mV}$ (with all the rest dc voltages being fixed), the charge qubit is first-order insensitive to the low-frequency charge noise and thus has the longest coherence [32], as shown below.

We then use the two-tone qubit spectroscopy to demonstrate the ac Stark effect and calibrate the average intra-resonator photon number $\bar{n}$. Keeping $V_{rg} = V_{ss}$ on the sweet spot and the drive power P_d low, we scan both the drive frequency f_d and the probe power P_p. In this scenario, $\bar{n}$ increases with the increasing P_p and the qubit frequency f_q shifts under the ac Stark effect [31]. Fig. 1f gives a series of curves of ϕ versus f_d with step-increased P_p. The detected f_q is red-shifted by $\delta f_{ac} \approx -6\,\text{MHz}$ when P_p (from the vector network analyzer) is increased from $-20\,\text{dBm}$ to $0\,\text{dBm}$. This shift is related to the average intra-resonator photon number $\bar{n}$

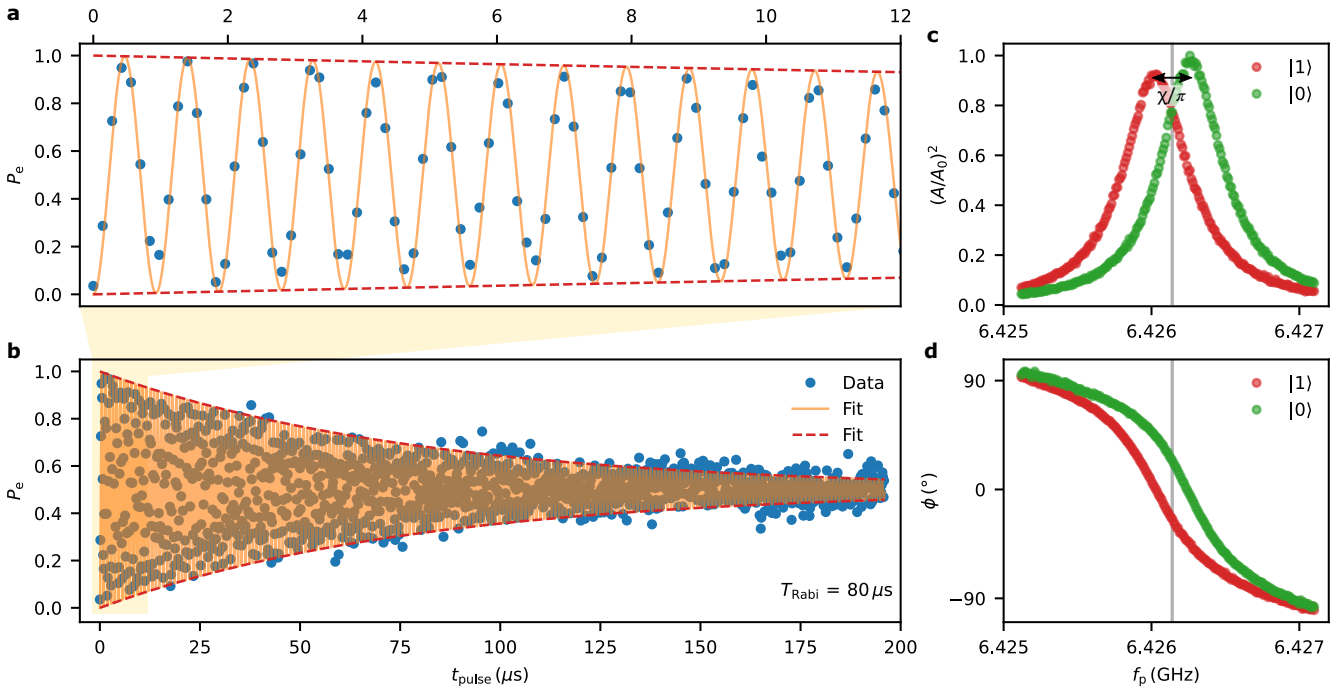

Fig. 2. Real-time control and readout of the electron-on-solid-neon (eNe) charge qubit. The qubit is operated on the sweet spot pointed by the yellow arrow in Fig. 1e. **a** and **b**, Observation of Rabi oscillations in a short and long time scale. The excited-state population P_e is plotted versus the microwave pulse duration t_{pulse} with a fixed amplitude and qubit frequency. The orange solid curve fits the exponentially decaying sinusoidal oscillations and the red dashed curve fits the exponentially decaying envelop. The fitted Rabi decay time is $T_{Rabi} = 80\,\mu$s. **c**, Normalized transmission amplitude $(A/A_0)^2$ versus the probe frequency f_p when the qubit is in the ground state $|0\rangle$ or excited state $|1\rangle$. The grey line corresponds to $f_p = f_r$, where f_r is the bare resonator frequency. The measured state-dependent dispersive shift is $\chi/2\pi = -0.13$ MHz. **d**, Transmission phase ϕ versus f_p when the qubit is on $|0\rangle$ or $|1\rangle$.

by $\delta f_{ac} = \chi\bar{n}/\pi$ [31]. Through this measurement, and the measurement of χ (see below), we know that a probe power $P_p < -13$ dBm ≈ 0.05 mW (about -135 dBm reaching the sample) corresponds to $\bar{n} < 1$.

State control and readout

We perform the real-time state control and readout on the eNe qubit in the dispersive regime. The qubit states are prepared by Gaussian microwave pulses with a fixed frequency f_q, a fixed amplitude A, and a variable pulse duration t_{pulse}. With increasing t_{pulse}, the qubit state, detected by the dispersive readout [18], oscillates between $|0\rangle$ and $|1\rangle$, known as the Rabi oscillations [33]. We operate the qubit on the sweet spot pointed by the yellow arrow in Fig. 1e. The observed Rabi oscillations are shown in Fig. 2a and 2b, plotted in a short and long time scale, respectively. The Rabi decay time $T_{Rabi} = 80\,\mu$s can be obtained by an exponential fit to the envelope of oscillatory population P_e in the excited state in the large time scale. Such a long T_{Rabi} indicates both a long relaxation time T_1 and a long pure-dephasing time T_φ, the latter of which is related to the total coherence time T_2 via $T_2^{-1} = (2T_1)^{-1} + T_\varphi^{-1}$. Theoretically, in the absence of inhomogeneous broadening and under a strong driving electric field, T_{Rabi} is related to T_1 and T_φ by $1/T_{Rabi} = 3/(4T_1) + 1/(2T_\varphi)$ [34,35].

The qubit readout follows the standard dispersive readout scheme, where the qubit states are inferred from measuring the phase or amplitude shift of the transmission $S_{21}(f_p)$ through the resonator. As shown in Fig. 2c and 2d, the resonator frequency is dispersively shifted to $f_r + \chi/2\pi$ or $f_r - \chi/2\pi$, when the qubit is in the excited state $|1\rangle$ or ground state $|0\rangle$. Here on the sweet spot, we have $\chi/2\pi = -0.13$ MHz. The dispersive readout has the highest contrast by fixing the probe frequency f_p at the bare resonance frequency f_r indicated by the gray line, where the phase separation between $|0\rangle$ and $|1\rangle$ is maximal.

Relaxation and coherence times

We now find the characteristic times of the eNe qubit, *i.e.*, the relaxation time T_1, the total dephasing (Ramsey) time T_2^*, and the total coherence time (after Hahn echoes) T_{2E}. These characteristic times provide the key measure of the single-qubit performance.

The total relaxation (decay) rate $T_1^{-1} = \Gamma = \Gamma_R + \Gamma_{NR}$ is the sum of radiative decay rate $\Gamma_R = \kappa g^2/\Delta^2$, which is determined by the Purcell effect [36,37], and nonradiative decay rate Γ_{NR}. It can be obtained by driving the qubit onto the excited state, waiting a variable delay time t_{delay} before readout, and observing an exponential decay of the excited-state population P_e with the increasing t_{delay}. On

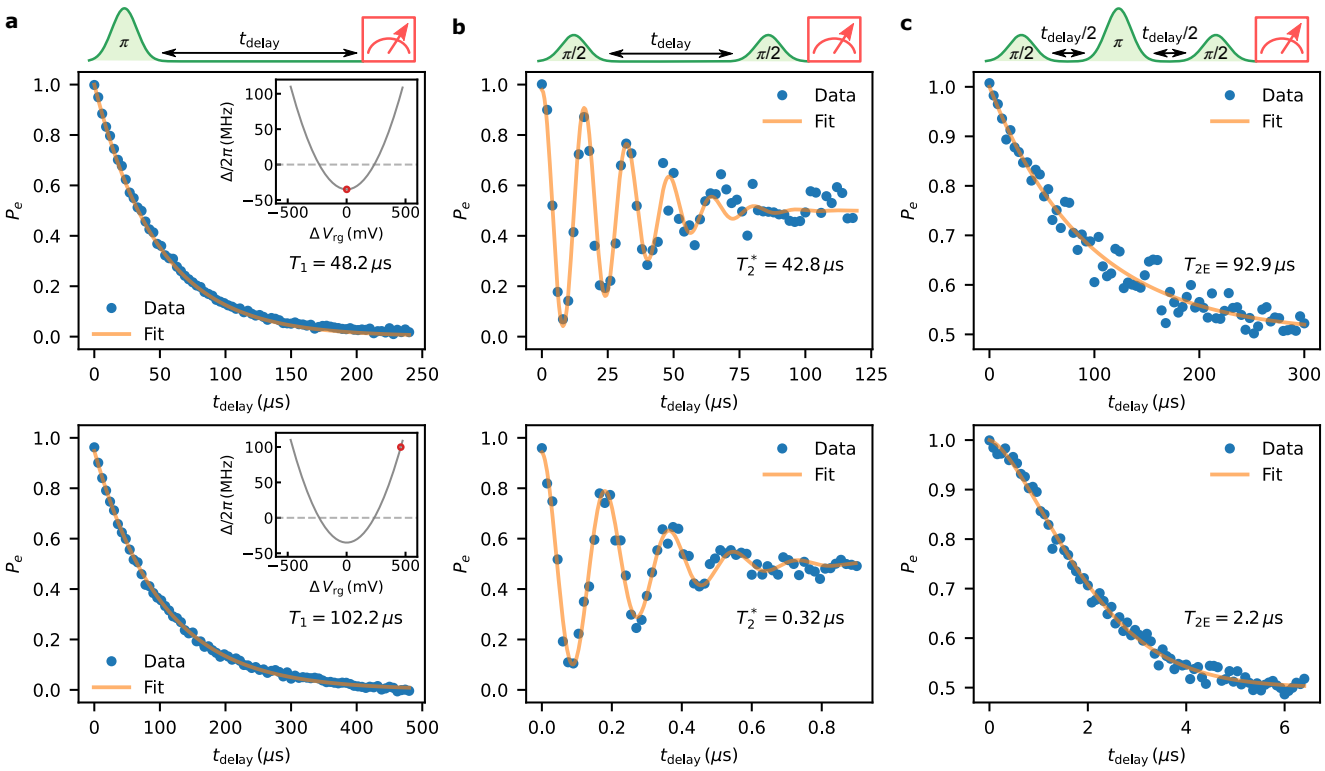

Fig. 3. Time-domain characterization of the electron-on-solid-neon (eNe) charge qubit. **a**, Relaxation time measurements of the qubit on (upper panel) and off (lower panel) the sweet spot. Excited-state population P_e is plotted versus the delay time t_{delay} between the readout pulse and a π-gate pulse. The sweet spot is at the minimum of the qubit spectrum detuned by $\Delta/2\pi = -34.7$ MHz from the bare resonator frequency and the non-sweet spot is chosen at a point with large slope on the qubit spectrum detuned by $\Delta/2\pi = 100$ MHz, as indicated by the circles in the insets. The fitted $T_1 = 48.2\,\mu$s and $102.2\,\mu$s on and off the sweet spot respectively. **b**, Ramsey-fringe measurements of the qubit on and off the sweet spot. P_e is plotted versus the delay time t_{delay} between two $\pi/2$-gate pulses. The fitted $T_2^* = 42.8\,\mu$s and $0.32\,\mu$s on and off the sweet spot respectively. **c**, Hahn-echo measurements of the qubit on and off the sweet spot. P_e is plotted versus the delay time t_{delay} between two $\pi/2$-gate pulses and separated by a π-gate pulse in the middle. The fitted $T_{2E} = 92.9\,\mu$s and $2.2\,\mu$s on and off the sweet spot, respectively.

the sweet spot, the measured T_1 is $48.2\,\mu$s, as shown in the upper panel of Fig. 3a. With the known values of g, κ, and $\Delta/2\pi = -34.7$ MHz on the sweet spot, we find a radiative decay time $\Gamma_R^{-1} = 78.7\,\mu$s and nonradiative decay time $\Gamma_{NR}^{-1} = 125\,\mu$s. This suggests that the Purcell-limited radiative decay is the dominant decay channel here. We verify this by purposely moving away from the sweet spot to a point with a larger detuning, $\Delta/2\pi = 100$ MHz. It gives an even longer T_1 of $102.2\,\mu$s, as shown in the lower panel of Fig. 3a, which agrees with the sum of the estimated Γ_R at this detuning and the Γ_{NR} above.

On the sweet spot, the first-order insensitivity of the qubit frequency to the low-frequency charge noise yields an exceedingly long total dephasing time T_2^* and a coherence time T_{2E} after a Hahn echo. In the Ramsey fringe measurement, two $\pi/2$ pulses are separated by a variable delay t_{delay}. A fit gives a $T_2^* = 42.8\,\mu$s, as shown in the upper panel of Fig. 3b. To our knowledge, this is the longest charge qubit dephasing time ever observed, compared with all the existing semiconductor quantum-dot and superconducting CPB charge qubits [2,3,10,38]. The remaining decoherence noise can be partially suppressed by applying echo pulses. In the Hahn echo experiment, with one π pulse inserted between the two $\pi/2$ pulses, we achieve an echo coherence time $T_{2E} = 92.9\,\mu$s, which almost equals $2T_1$, as shown in the upper panel of Fig. 3c. This means that the decoherence on the sweet spot is dominated by the relaxation and any decoherence sources that cannot be mitigated by the Hahn echo must be much slower. These results suggest that solid Ne can indeed serve as a superior host material for electron qubits [39]. As a comparison, we purposely move off the sweet spot to a point more sensitive to charge noise at 100 MHz detuning. The observed T_2^* decreases to $0.32\,\mu$s and T_{2E} decreases to $2.2\,\mu$s, as shown in the lower panels of Fig. 3b and 3c.

Readout and gate fidelities

We then determine the readout and gate fidelities in the eNe qubit system. In the absence of a quantum-limited amplifier, we wish to push for the highest possible single-shot readout fidelity by operating a qubit with the longest possible T_1 and still acceptable T_2 on the

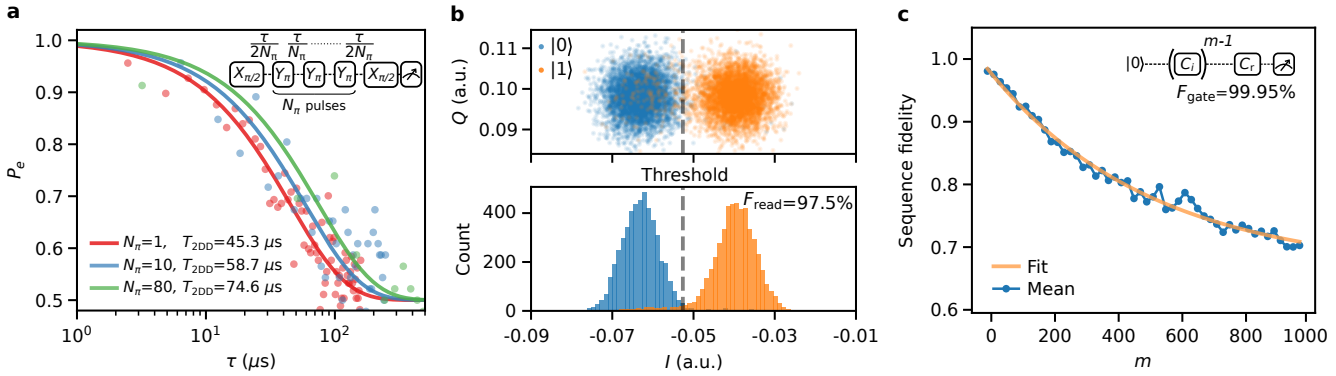

Fig. 4. Coherence improvement by dynamical decoupling and measurements of single-shot readout fidelity and one-qubit gate fidelity. **a**, Excited-state population P_e versus the total evolution time τ for different numbers of CPMG dynamical-decoupling pulses. With $N_\pi = 80$, $T_{2DD} = 74.6\,\mu$s is nearly 20 times longer than the $T_2^* = 3.9\,\mu$s for this qubit. **b**, Single-shot distribution of readout values when the qubit is prepared on $|0\rangle$ or $|1\rangle$, in the absence of a quantum-limited amplifier. The overlapped area yields a single-shot readout fidelity $F_{read} = 97.5\%$. **c**, One-qubit gate fidelity measurement using the Clifford-based randomized benchmarking technique. The mean data are averaged over 75 random sequences. An exponential fit of the sequence fidelity versus the number of Clifford gates M yields an average gate fidelity $F_{gate} = 99.95\%$.

sweet spot. We trap and select a different electron that has a much larger detuning, $\Delta/2\pi = -270$ MHz on the sweet spot, to more strongly suppress the Purcell-limited radiative decay. We find that this qubit has a $T_1 = 88.4\,\mu$s and $T_2^* = 3.9\,\mu$s on the sweet spot. While the T_2^* of this qubit is about one order of magnitude shorter than the last qubit, we take this chance to demonstrate using the Carr-Purcell-Meiboom-Gill (CPMG) dynamical-decoupling (DD) pulse sequence to improve the qubit coherence by nearly 20 times. As shown in Fig. 4a, for the number of π pulses $N_\pi = 1$ (equivalent to applying one echo pulse), we have $T_{2DD} = T_{2E} = 45.3\,\mu$s, for $N_\pi = 10$, $T_{2DD} = 58.7\,\mu$s, and for $N_\pi = 80$, $T_{2DD} = 74.6\,\mu$s. A large number of N_π makes the coherence time approach the order of 0.1 ms again.

The sharp contrast of microwave transmission with respect to the different qubit states in the dispersive readout scheme, as described in Fig. 2d above, can be used to define the single-shot readout fidelity. Fig. 4b shows the distribution of single-shot readout values when the qubit is prepared on $|0\rangle$ or $|1\rangle$ respectively. It yields a single-shot readout fidelity $F_{read} = 97.5\%$ [40], without using a quantum-limited amplifier. This is a remarkable result compared with $F_{read} = 94.7\%$ of superconducting transmon qubits with a similar amplification chain [23,41].

The one-qubit gate fidelity for this qubit on the sweet spot is characterized by the Clifford-based randomized benchmarking technique [24]. In this protocol, a Clifford gate sequence with an increasing number of gates M is applied to the qubit in the ground state. The sequence contains $M - 1$ Clifford gates C_i that are randomly chosen from the Clifford group, followed by a recovery Clifford gate C_r, which (ideally) sets the qubit back to the ground state. The exponential decay of the sequence fidelity versus M gives an estimate of the average one-qubit gate fidelity F_{gate}. As shown in Fig. 4c, we achieve a $F_{gate} = 99.95\%$ that is well above the threshold for quantum error correction with surface codes [25].

Two qubits strong coupling

To build a universal quantum computer, a two-qubit entangling gate is necessary [26]. Beyond the already realized single-qubit operations, we are able to load two qubits on the same trap and spectroscopically bring them on and off resonance with the resonator and show strong coupling for each of them. This is the first step toward achieving two-qubit entangling gates for the eNe charge qubits in a cQED architecture.

To demonstrate two-qubit tuning in our current device, we need at least two tuning voltages, which we choose to be the (offset) resonator voltage ΔV_r and resonator-guard voltage ΔV_{rg}. Since the two qubits have different voltage dependence of their qubit frequencies f_{q1} and f_{q2}, we can individually or simultaneously achieve the strong coupling between the two qubits and the resonator. We call the qubit with larger coupling strength as qubit-1 and the other as qubit-2. The upper row of Fig. 5 displays our experimental observation and the lower row displays our theoretical calculation. Fig. 5a demonstrates how the two qubits can be brought onto resonance with the resonator by tuning both ΔV_r and ΔV_{rg}. We measure the normalized transmission amplitude $(A/A_0)^2$ of the resonator at the bare resonance frequency. The two dark lines indicate the qubit-resonator on-resonance conditions, $f_{q1} = f_r$ and $f_{q2} = f_r$, respectively. The parameter space $(\Delta V_{rg}, \Delta V_r)$ is divided by the two dark lines into four regions: $(f_{q1}, f_{q2}) > f_r$, $(f_{q1}, f_{q2}) < f_r$, $f_{q1} > f_r > f_{q2}$, and $f_{q1} < f_r < f_{q2}$. A notable feature is that $(A/A_0)^2$ is smaller in the $(f_{q1}, f_{q2}) > f_r$ and $(f_{q1}, f_{q2}) < f_r$ two regions, compared with the other two regions. This is expected from strong coupling of two qubits with a resonator. In these two regions, both qubits push the resonator frequency in the same

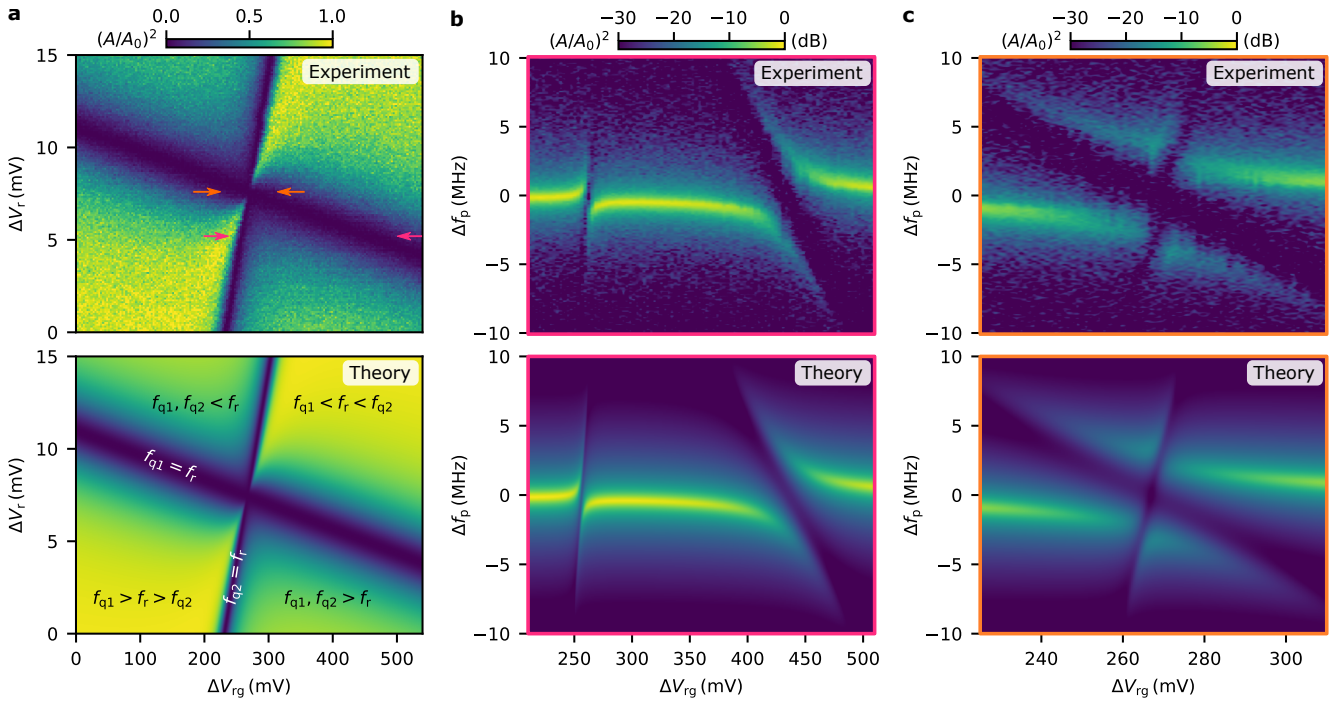

Fig. 5. Spectroscopic studies of two qubits coupled with the resonator. Upper row shows the experimental observation and lower row shows the theoretical calculation. The qubit with larger or smaller coupling strength is labeled as qubit-1 or qubit-2, respectively. **a**, Spectral tuning of two qubits. The microwave transmission amplitude $(A/A_0)^2$ through the resonator probed at the bare resonator frequency $f_p = f_r$ is plotted against the (offset) resonator voltage ΔV_r and resonator-guard voltage ΔV_{rg}. The parameter space (ΔV_{rg}, ΔV_r) is divided into four regions by the two dark lines that correspond to each qubit being individually on resonance with the resonator. The relations between f_{q1}, f_{q2} and f_r in the four regions and along the two lines are labeled in the lower panel. At the crossing of two dark lines marked by the orange arrows, the two qubits are simultaneously on resonance with the resonator. **b**, $(A/A_0)^2$ versus $\Delta f_p = f_p - f_r$ and ΔV_{rg} along the line indicated by the pink arrows in **a**, where the two qubits can be individually on resonance with the resonator. **c**, $(A/A_0)^2$ versus Δf_p and ΔV_{rg} along the line indicated by the orange arrows in **a**, where the two qubits can be simultaneously on resonance with the resonator.

direction, resulting a larger resonator frequency shift and thus a smaller transmission amplitude, as verified by the theoretical calculation as well.

Fig. 5b shows the system spectrum when the two qubits are individually brought onto resonance with the resonator by a tunable ΔV_{rg} and a fixed $\Delta V_r = 5.2\,\mathrm{mV}$, as indicated by the magenta arrows in Fig. 5a. We can retrieve the coupling strength $g_1/2\pi = 3.6\,\mathrm{MHz}$, $g_2/2\pi = 1.8\,\mathrm{MHz}$, and the qubit linewidth $\gamma_1/2\pi = 1.5\,\mathrm{MHz}$, $\gamma_2/2\pi = 1.6\,\mathrm{MHz}$ from the individual vacuum Rabi splitting. Fig. 5c shows the system spectrum when the two qubits are simultaneously brought onto resonance with the resonator by a tunable ΔV_{rg} and another fixed $\Delta V_r = 7.4\,\mathrm{mV}$, as indicated by the orange arrows in Fig. 5a. At $\Delta V_{rg} = 267\,\mathrm{mV}$, the resonator is simultaneously hybridized with both qubits.

It is known that an interacting system of two qubits and one resonator can be described by the Tavis-Cummings model [42]. With the known frequencies, detunings, coupling strengths, and linewidths from above, utilizing the input-output formalism [43], we can theoretically calculate the normalized transmission amplitude $(A/A_0)^2$ through the system. Comparing the experimental (upper row) and theoretical (lower row) results in Fig. 5, we observe a nearly perfect agreement between experiment and theory.

Discussion and outlook

While our measured coherence time for an eNe qubit has approached 0.1 ms, we believe that it can be further improved by optimizing our device design, drive scheme, and solid-Ne growth procedure. Solely from the material perspective, we do not foresee a practical limit on the charge-qubit coherence time in this system, though theoretical calculation can be done to find out the ultimate decoherence due to thermal phonons or quantum zero-point motion of Ne atoms [39,44–46].

The anharmonicity α, defined as the frequency difference between the $|g\rangle \rightarrow |e\rangle$ and $|e\rangle \rightarrow |f\rangle$ transitions with $|f\rangle$ being the second excited state, is a critical parameter for the gate time. A larger α ensures a shorter gate time [33]. For our qubit, α is estimated to be greater than 1 GHz, based on the large detuning range and strong pumping power that we have explored. We were not able to observe a $|g\rangle \rightarrow |f\rangle$ two-photon transition or a $|e\rangle \rightarrow |f\rangle$ one-photon transition after preparing the qubit on $|e\rangle$. We shall note that even for an infinite α, which

corresponds to an ideal two-level system, the theoretical dispersive shift would be $\chi = g^2/\Delta = -0.152$ MHz, which is quite close to our measured -0.13 MHz. This is another evidence that our α can be extraordinarily large, $|\alpha| \gg |\Delta|$.

Lastly, to achieve two-qubit entangling gates in the cQED architecture, we need to push on from the resonant strong regime into the dispersive strong regime. This requires larger g/γ and g/κ [47]. In light of the observed $\gamma/2\pi \lesssim 0.02$ MHz at the charge sweet spot, g/γ already satisfies the strong dispersive requirement. To keep fast operations, the resonator linewidth κ from the input-output coupling cannot be much smaller than the current $\kappa/2\pi = 0.46$ MHz. Optimally, the coupling strength g should be enhanced by about ten times. This may be accomplished by using high kinetic-inductance superconducting materials for the on-chip resonator [48]. Realization of two-qubit entangling gates based on the eNe charge qubit platform will establish a further milestone toward universal quantum computing [26].

ACKNOWLEDGMENTS

This work was performed at the Center for Nanoscale Materials, a U.S. Department of Energy Office of Science User Facility, and supported by the U.S. Department of Energy, Office of Science, under Contract No. DE-AC02-06CH11357. D.J., X.L., and Q.C. acknowledge support from Argonne National Laboratory Directed Research and Development (LDRD). D.J. and X.Zhou acknowledge support from the Julian Schwinger Foundation for Physics Research. This work was partially supported by the University of Chicago Materials Research Science and Engineering Center, which is funded by the National Science Foundation under award number DMR-2011854. This work made use of the Pritzker Nanofabrication Facility of the Institute for Molecular Engineering at the University of Chicago, which receives support from SHyNE, a node of the National Science Foundation National Nanotechnology Coordinated Infrastructure (NSF NNCI-1542205). D.I.S. and B.D. acknowledge support from the National Science Foundation DMR grant DMR-1906003. D.I.S. acknowledges support from the U.S. Department of Energy, Office of Science, National Quantum Information Science Research Centers. G.Y. acknowledges supports from the National Science Foundation under Cooperative Agreement PHY-2019786 (the NSF AI Institute for Artificial Intelligence and Fundamental Interactions). D.J. thanks Anthony J. Leggett for inspiring discussions. The qubit manipulation and measurement in this work utilized the highly efficient and effective OPX+, Octave, and QDAC-II made by Quantum Machines and QDevil.

*These authors contributed equally to this work.
†Email: dschus@stanford.edu
‡Email: dfjin@nd.edu

[1] T. D. Ladd, F. Jelezko, R. Laflamme, Y. Nakamura, C. Monroe, and J. L. O'Brien, "Quantum computers," Nature **464**, 45–53 (2010).
[2] A. Chatterjee, P. Stevenson, S. De Franceschi, A. Morello, N. P. de Leon, and F. Kuemmeth, "Semiconductor qubits in practice," Nat. Rev. Phys. **3**, 157–177 (2021).
[3] I. Siddiqi, "Engineering high-coherence superconducting qubits," Nat. Rev. Mater. **6**, 875–891 (2021).
[4] L. Viola, E. Knill, and S. Lloyd, "Dynamical decoupling of open quantum systems," Phys. Rev. Lett. **82**, 2417–2421 (1999).
[5] J. T. Muhonen, J. P. Dehollain, A. Laucht, F. E. Hudson, R. Kalra, T. Sekiguchi, K. M. Itoh, D. N. Jamieson, J. C. McCallum, A. S. Dzurak, and A. Morello, "Storing quantum information for 30 seconds in a nanoelectronic device," Nat. Nanotechnol. **9**, 986–991 (2014).
[6] M. Veldhorst, J. C. Hwang, C. H. Yang, A. W. Leenstra, B. De Ronde, J. P. Dehollain, J. T. Muhonen, F. E. Hudson, K. M. Itoh, A. Morello, and A. S. Dzurak, "An addressable quantum dot qubit with fault-tolerant control-fidelity," Nat. Nanotechnol. **9**, 981–985 (2014).
[7] L. B. Nguyen, Y. H. Lin, A. Somoroff, R. Mencia, N. Grabon, and V. E. Manucharyan, "High-Coherence Fluxonium Qubit," Phys. Rev. X **9**, 041041 (2019).
[8] A. Somoroff, Q. Ficheux, R. A. Mencia, H. Xiong, R. V. Kuzmin, and V. E. Manucharyan, "Millisecond coherence in a superconducting qubit," arXiv:2103.08578 (2021).
[9] A. P. Place, L. V. Rodgers, P. Mundada, B. M. Smitham, M. Fitzpatrick, Z. Leng, A. Premkumar, J. Bryon, A. Vrajitoarea, S. Sussman, G. Cheng, T. Madhavan, H. K. Babla, X. H. Le, Y. Gang, B. Jäck, A. Gyenis, N. Yao, R. J. Cava, N. P. de Leon, and A. A. Houck, "New material platform for superconducting transmon qubits with coherence times exceeding 0.3 milliseconds," Nat. Commun. **12**, 1779 (2021).
[10] C. Wang, X. Li, H. Xu, Z. Li, J. Wang, Z. Yang, Z. Mi, X. Liang, T. Su, C. Yang, G. Wang, W. Wang, Y. Li, M. Chen, C. Li, K. Linghu, J. Han, Y. Zhang, Y. Feng, Y. Song, T. Ma, J. Zhang, R. Wang, P. Zhao, W. Liu, G. Xue, Y. Jin, and H. Yu, "Towards practical quantum computers: transmon qubit with a lifetime approaching 0.5 milliseconds," npj Quantum Inf. **8**, 3 (2022).
[11] P. Stano and D. Loss, "Review of performance metrics of spin qubits in gated semiconducting nanostructures," Nat. Rev. Phys. **4**, 672–688 (2022).
[12] A. J. Heinrich, W. D. Oliver, L. M. Vandersypen, A. Ardavan, R. Sessoli, D. Loss, A. B. Jayich, J. Fernandez-Rossier, A. Laucht, and A. Morello, "Quantum-coherent nanoscience," Nat. Nanotechnol. **16**, 1318–1329 (2021).
[13] M. A. Nielsen and I. L. Chuang, *Quantum Computation and Quantum Information* (Cambridge University Press, 2010).
[14] D. Kim, D. R. Ward, C. B. Simmons, J. K. Gamble, R. Blume-Kohout, E. Nielsen, D. E. Savage, M. G. Lagally, M. Friesen, S. N. Coppersmith, and M. A. Eriksson, "Microwave-driven coherent operation of a semiconductor quantum dot charge qubit," Nat. Nanotechnol. **10**, 243–247 (2015).
[15] J. Yoneda, K. Takeda, T. Otsuka, T. Nakajima, M. R. Delbecq, G. Allison, T. Honda, T. Kodera, S. Oda, Y. Hoshi, *et al.*, "A quantum-dot spin qubit with coherence limited by charge noise and fidelity higher than 99.9%," Nat. Nanotechnol. **13**, 102–106 (2018).
[16] A. Osman, J. Simon, A. Bengtsson, S. Kosen, P. Krantz, D. P. Lozano, M. Scigliuzzo, P. Delsing, J. Bylander, and A. Fadavi Roudsari, "Simplified Josephson-junction fabrication process for reproducibly high-performance superconducting qubits," Appl. Phys. Lett. **118**, 064002 (2021).
[17] Y. A. Pashkin, O. Astafiev, T. Yamamoto, Y. Nakamura, and J. S. Tsai, "Josephson charge qubits: A brief review," Quantum Inf. Process. **8**, 55–80 (2009).
[18] A. Blais, A. L. Grimsmo, and A. Wallraff, "Circuit quantum electrodynamics," Rev. Mod. Phys. **93**, 025005 (2021).
[19] X. Zhou, G. Koolstra, X. Zhang, G. Yang, X. Han, B. Dizdar, X. Li, D. Ralu, W. Guo, K. W. Murch, D. I. Schuster, and D. Jin,

"Single electrons on solid neon as a solid-state qubit platform," Nature **605**, 46–50 (2022).
[20] V. Zavyalov, I. Smolyaninov, E. Zotova, A. Borodin, and S. Bogomolov, "Electron states above the surfaces of solid cryodielectrics for quantum-computing." J. Low Temp. Phys. **138**, 415–420 (2005).
[21] C. D. Wilen, S. Abdullah, N. A. Kurinsky, C. Stanford, L. Cardani, G. D'Imperio, C. Tomei, L. Faoro, L. B. Ioffe, C. H. Liu, A. Opremcak, B. G. Christensen, J. L. DuBois, and R. McDermott, "Correlated charge noise and relaxation errors in superconducting qubits," Nature **594**, 369–373 (2021).
[22] P. Leiderer, K. Kono, and D. Rees, in *Proc. 11th International Conference on Cryocrystals and Quantum Crystals*, edited by S. Vasiliev (2016) pp. 67–67.
[23] F. Mallet, F. R. Ong, A. Palacios-Laloy, F. Nguyen, P. Bertet, D. Vion, and D. Esteve, "Single-shot qubit readout in circuit quantum electrodynamics," Nat. Phys. **5**, 791–795 (2009).
[24] E. Knill, D. Leibfried, R. Reichle, J. Britton, R. B. Blakestad, J. D. Jost, C. Langer, R. Ozeri, S. Seidelin, and D. J. Wineland, "Randomized benchmarking of quantum gates," Phys. Rev. A **77**, 012307 (2008).
[25] A. G. Fowler, M. Mariantoni, J. M. Martinis, and A. N. Cleland, "Surface codes: Towards practical large-scale quantum computation," Phys. Rev. A **86**, 032324 (2012).
[26] D. P. Divincenzo, D. Bacon, J. Kempe, G. Burkard, and K. B. Whaley, "Universal quantum computation with the exchange interaction," Nature **408**, 339–342 (2000).
[27] G. Koolstra, G. Yang, and D. I. Schuster, "Coupling a single electron on superfluid helium to a superconducting resonator," Nat. Commun. **10**, 5323 (2019).
[28] R. T. Jacobsen, S. G. Penoncello, and E. W. Lemmon, "Thermodynamic properties of cryogenic fluids," in *Thermodynamic Properties of Cryogenic Fluids* (Springer, 1997) pp. 31–287.
[29] F. Mugele, U. Albrecht, P. Leiderer, and K. Kono, "Possible correlation effects of surface state electrons on a solid hydrogen film," J. Low Temp. Phys. **89**, 743–746 (1992).
[30] D. I. Schuster, A. Fragner, M. I. Dykman, S. A. Lyon, and R. J. Schoelkopf, "Proposal for manipulating and detecting spin and orbital states of trapped electrons on helium using cavity quantum electrodynamics," Phys. Rev. Lett. **105**, 040503 (2010).
[31] D. I. Schuster, A. Wallraff, A. Blais, L. Frunzio, R. S. Huang, J. Majer, S. M. Girvin, and R. J. Schoelkopf, "ac Stark shift and dephasing of a superconducting qubit strongly coupled to a cavity field," Phys. Rev. Lett. **94**, 123602 (2005).
[32] D. Vion, A. Aassime, A. Cottet, P. Joyez, H. Pothier, C. Urbina, D. Esteve, and M. H. Devoret, "Manipulating the quantum state of an electrical circuit," Science **296**, 886–889 (2002).
[33] P. Krantz, M. Kjaergaard, F. Yan, T. P. Orlando, S. Gustavsson, and W. D. Oliver, "A quantum engineer's guide to superconducting qubits," Appl. Phys. Rev. **6**, 021318 (2019).
[34] L. Allen and J. H. Eberly, *Optical Resonance and Two-Level Atoms* (Dover, New York, 1987).
[35] R. Bianchetti, S. Filipp, M. Baur, J. M. Fink, M. Göppl, P. J. Leek, L. Steffen, A. Blais, and A. Wallraff, "Dynamics of dispersive single-qubit readout in circuit quantum electrodynamics," Phys. Rev. A **80**, 043840 (2009).
[36] E. M. Purcell, "Spontaneous emission probabilities at radio frequencies," Phys. Rev. **69**, 681 (1946).
[37] E. A. Sete, J. M. Gambetta, and A. N. Korotkov, "Purcell effect with microwave drive: Suppression of qubit relaxation rate," Phys. Rev. B **89**, 104516 (2014).
[38] J. Verjauw, R. Acharya, J. Van Damme, T. Ivanov, D. P. Lozano, F. Mohiyaddin, D. Wan, J. Jussot, A. Vadiraj, M. Mongillo, *et al.*, "Path toward manufacturable superconducting qubits with relaxation times exceeding 0.1 ms," arXiv:2202.10303 (2022).
[39] Q. Chen, I. Martin, L. Jiang, and D. Jin, "Electron spin coherence on a solid neon surface," Quantum Sci. and Technol. **7**, 045016 (2022).
[40] J. Gambetta, W. A. Braff, A. Wallraff, S. M. Girvin, and R. J. Schoelkopf, "Protocols for optimal readout of qubits using a continuous quantum nondemolition measurement," Phys. Rev. A **76**, 012325 (2007).
[41] L. Stefanazzi, K. Treptow, N. Wilcer, C. Stoughton, C. Bradford, S. Uemura, S. Zorzetti, S. Montella, G. Cancelo, S. Sussman, A. Houck, S. Saxena, H. Arnaldi, A. Agrawal, H. Zhang, C. Ding, and D. I. Schuster, "The QICK (Quantum Instrumentation Control Kit): Readout and control for qubits and detectors," Rev. Sci. Instrum. **93**, 044709 (2022).
[42] M. Tavis and F. Cummings, "Exact solution for an n-molecule—radiation-field hamiltonian," Phys. Rev. **170**, 379–384 (1968).
[43] D. F. Walls and G. J. Milburn, *Quantum optics* (Springer Science & Business Media, 2007).
[44] M. I. Dykman, P. M. Platzman, and P. Seddighrad, "Qubits with electrons on liquid helium," Phys. Rev. B **67**, 155402 (2003).
[45] G. L. Pollack, "The Solid State of Rare Gases," Rev. Mod. Phys. **36**, 748 (1964).
[46] M. L. Klein and J. A. Venables, *Rare Gas Solids*, Vol. I (Academic, New York, 1976).
[47] D. I. Schuster, *Circuit Quantum Electrodynamics*, Ph.D. thesis, Yale University (2007).
[48] A. Shearrow, G. Koolstra, S. J. Whiteley, N. Earnest, P. S. Barry, F. J. Heremans, D. D. Awschalom, E. Shirokoff, and D. I. Schuster, "Atomic layer deposition of titanium nitride for quantum circuits," Appl. Phys. Lett. **113**, 212601 (2018).